

Elucidation of differential mineralisation
on native and regenerated silk matrices

Swati Midha^a, Rohit Tripathi^a, Hua Geng^b, Peter D. Lee^b, Sourabh Ghosh^{a*}

^a Department of Textile Technology, Indian Institute of Technology, New Delhi, India

^b School of Materials, University of Manchester, Manchester M13 9PL, UK

***Corresponding author email:** sghosh08@textile.iitd.ac.in

All authors: Swati Midha, swati.mid@gmail.com; Rohit Tripathi, trohit3062@gmail.com; Hua Geng, hua.geng@postgrad.manchester.ac.uk; Peter D. Lee, peter.lee@manchester.ac.uk

Phone: 91-11-2659-1440

Fax: 91-11-2659-1103

Abstract

Bone mineralisation is a well-orchestrated procedure triggered by a protein-based template inducing the nucleation of hydroxyapatite (HA) nanocrystals on the matrix. In an attempt to fabricate superior nanocomposites from silk fibroin, textile braided structures made of natively spun fibres of *Bombyx mori* silkworm were compared against regenerated fibroin (lyophilised and films) underpinning the influence of intrinsic properties of fibroin matrices on HA nucleation. We found that native braids could bind Ca^{2+} ions through electrostatic attraction, which initiated the nucleation and deposition of HA, as evidenced by discrete shift in amide peaks *via* ATR-FTIR. This phenomenon also suggests the involvement of amide linkages in promoting HA nucleation on fibroin. Moreover, CaCl_2 -SBF immersion of native braids resulted in preferential growth of HA along the c-axis, forming needle-like nanocrystals and possessing Ca/P ratio comparable to commercial HA. Though regenerated lyophilised matrix also witnessed prominent peak shift in amide linkages, HA growth was restricted to (211) plane only, albeit at a significantly lower intensity than braids. Regenerated films, on the other hand, provided no crystallographic evidence of HA deposition within 7 days of SBF immersion. The present work sheds light on the primary fibroin structure of *B.mori* which probably plays a crucial role in regulating template-induced biominerallisation on the matrix. We also found that intrinsic material properties such as surface roughness, geometry, specific surface area, tortuosity and secondary conformation exert influence in modulating the extent of mineralisation. Thus our work generates useful insights and warrants future studies to further investigate the potential of bone mimetic, silk/mineral nanocomposite matrices for orthopaedic applications.

Keywords: silk fibroin, mineralisation, hydroxyapatite, textile braid, simulated body fluid

1. Introduction

Bone is a complex nanocomposite consisting of organic–inorganic phases of collagen-hydroxyapatite (HA) crystals, where HA $[\text{Ca}_{10}(\text{PO}_4)_6(\text{OH})_2]$ measures 20–30 nm in width, 100 nm in length with 3–6 nm thickness [1], precisely embedded between longitudinally arranged collagen fibres such that HA is synthesized on the c-axis plane along the longitudinal axis of collagen [2]. In addition, HA exhibits intimate chemical bonding between the organic-inorganic elements with an overall poor crystallinity [2]. Growing interest in the development of biomimetic synthetic HA-based composites is primarily due to; (i) developing synthetic “analog” of HA to be able to precisely replicate the morphology and chemistry of bone tissue [3], (ii) HA coating on constructs for improving osteoconductivity and (iii) evaluating the bioactivity of novel materials by studying the nucleation and growth of “bone-like” apatite upon immersion in supersaturated fluids such as simulated body fluid (SBF) [4]. However, there are still gaps in understanding the nature of such depositions; surface features and crystallisation phase especially with respect to the morphology and chemistry of the base material.

Silk fibroin, another fibrous protein that closely mimics collagen type I of bone has gained popularity in tissue engineering due to interesting intrinsic properties such as resorbability [5], toughness [6], minimal immunogenicity [7,8], cytocompatibility with abundant polar, hydrophilic groups [9], strong chemical bonding with HA [10-13] and versatility in processing depending upon the target application.¹⁴ Silk fibroin template fabricated in the form of nano fibres [12], films [15], porous 3D matrices [16] and composites [17] exposed to supersaturated ions, SBF [4,10] or fetal bovine serum [11], have been tested before for HA deposition. Silk fibroin plays a crucial role in regulating the synthesis and growth of HA nanocrystals [18], as HA combines with fibroin through chemical interactions which have been identified by FTIR analyses whereby the strong chemical bonding between the two caused peak shifts in the amide bonds of fibroin, commonly referred to as the ‘blue shift’ [2]. However, majority of these stud-

ies have largely ignored the role of template chemistry of native fibroin in directing the nucleation and growth of HA. The primary reason could be that most of the studies used regenerated silk fibroin materials formed by the subsequent dissolution and re-assembly of native silkworm cocoons which tends to disrupt the original protein conformation [19]. Moreover, the role of different morphologies and other physical characteristics as a potential cause of large variations in the resultant mineralisation attained have not been addressed. In this study, we hypothesize that native silk fibroin will experience superior mineralisation in the presence of supersaturated solution, credited to the intact organization of the primary amino acid composition and structure. To test this hypothesis and understand the underlying chemical interactions governing the process of HA nucleation on fibroin matrix, we examined the change in the intrinsic properties of fibroin and thoroughly characterized HA crystallisation on the material surface initiated by incubating silk structures in simulated body fluid ($1.5 \times$ SBF).

Furthermore, there are theories which attribute the mineralisation potential of fibroin to the amorphous anionic bridges present between the β -sheets present within the structure [20]. In this study, Marelli *et al.* compared the hydrophobic chains in fibroin against the hydrophilic, electronegative chains and found apatite formation only in the hydrophilic fragments. They concluded that the differences in the mineralisation potential of silk fibroin were due to its constituent anionic chains which typically resembled the non-collagenous, anionic fragments of collagen type I. In another study, Kino *et al.* prepared regenerated silk fibroin films with varied calcium chloride contents and reported deposition of HA post-immersion in $1.5 \times$ SBF, but only in films possessing more than 3 wt% of calcium chloride relative to silk fibroin [15]. The reason was attributed to the presence of Ca^{2+} ions at a particular concentration which reportedly induced more \rightarrow -sheets in the fibroin structure [21] and such modified silk fibroin films demonstrated improved HA coating [15]. However, quantitative analysis of this varying β -sheet content was not done. Also, the reason as to why mineralisation could not be observed

on methanol treated pure fibroin films (without calcium chloride) which contained at least some amount of β -sheet content remained unexplained. Nevertheless, most studies have reported an additional requirement of either pre-exposure of fibroin or its association with calcium- and phosphate-based solutions to promote nucleation and growth of HA nanocrystals [12,13,16,22]. Whether it is the processing parameters during dissolution and reconstitution that disrupt the native structure of the fibroin chain; firstly by dissociating the specific amino acid chains and secondly by hampering their tendency to re-assemble the necessary β -sheet conformation, or if it is the inherent inert nature of fibroin chain that modulates the extent of mineralisation is still under wraps. These studies further highlighted the fact that our current understanding of the primary structure of fibroin is insufficient to elucidate the mineralisation capacity of silk fibroin in order to use it as a potential bone graft substitute [9].

Apart from the secondary conformation, there are other contributing factors that determine apatite formation on biomaterials including molecular size, surface chemistry, topography, surface charge, stiffness, target site and rate of *in situ* degradation which needs to be taken into account. For instance, hydrophobic crystalline fractions of silk fibroin with a 40 kDa MW are weak templates for mineralisation, whereas 2-10 kDa MW hydrophilic chains are strong templates [20]. Moreover, the specific surface area of the biomaterial plays a crucial role in determining the amount of apatite formation, as a larger hydrated layer of organic template with strong tendency for ion exchange facilitates higher precipitation of nanocrystalline HA [3]. Therefore, in the present study, we aim to address the following three specific questions with respect to *in vitro* mineralisation potential of silk fibroin; (i) the role of fibroin as an osteogenic substrate (in regenerated versus native form) in regulating nanocrystalline apatite synthesis, (ii) whether change in 3D morphology (lyophilised versus braid) influences HA deposition on fibroin and (iii) whether the modified 3D morphology and resultant variation in the intrinsic material properties modulate the extent of mineralisation. To the best of our

knowledge, this is the first study to provide an indepth analysis of the difference in mineralisation in silk fibroin matrices between the native and regenerated fibres. We hypothesized that by inducing morphological changes in the fibroin structure, we could modulate the material properties which will eventually enhance control over the nucleation and growth of the HA phase. In order to characterize the mineralisation quotient, we used a combination of several sophisticated analytical techniques combining high end imaging and compositional analysis of the fabricated matrices to generate correlation between the material properties and the resultant mineralisation. We believe that understanding the process of mineralisation on the hierarchical assembly of fibroin will provide some innovative ideas for fabricating functional silk-based materials with customized morphology and chemistry best suited to promote biominerallisation *in situ*.

2. Materials and methods

2.1 Isolation of silk fibroin solution

12 tex 2-ply *B.mori* silk yarn were procured from Starling Mills Pvt. Ltd., Malda district, West Bengal, India. Silk solution was prepared directly from the fibres according to a protocol used routinely [23,24]. Briefly, 5 gm of *B.mori* fibres were weighed and cut into fine pieces, followed by boiling in 0.02 M Na₂CO₃ for 30 min to remove sericin. The fibres were then thoroughly rinsed in deionized water to isolate fibroin protein. Once completely dried, fibres were solubilized in 9.3M LiBr solution at 60 °C for 4 h. Fibroin-LiBr solution was dialysed using Slide-A-Lyzer cassette (Thermo, molecular weight cut off 3500) yielding 6.1 wt% solution of silk fibroin, which was stored at 4 °C until subsequent usage.

2.2 Preparation of regenerated silk fibroin matrices

Aqueous silk fibroin solution of the same concentration (i.e. 6.1 wt%) was used for the fabrication of both lyophilised matrices and 2D planar films.

2.2.1 Silk Films

To generate silk solution in the form of planar films, 2 ml of silk fibroin solution was pipetted over $10 \times 10 \text{ mm}^2$ teflon plates and dried at RT overnight. Post-drying, the films were immersed in sufficient volume of 80% ethanol for 2 h at RT in order to induce β -sheet crystallisation.

2.2.2 Lyophilised

A randomly porous three-dimensional (3D) morphology was obtained by lyophilizing fibroin solution. Approximately 10 ml of the solution was poured into a 30 cm^2 glass petri dish and frozen at -20°C in a refrigerator for 24 h. The resulting silk solution was then lyophilised to generate a 3D porous matrix, which was subsequently immersed in ethanol for 2 h to induce β -sheet crystallisation.

2.2.3 Silk Braids

Fibres of *B.mori* silk were fabricated into 3D braids using a 17 spindles Flat braiding machine type NG1/16-120 (August Herzog Maschinenfabrik GmbH & Co. KG, Germany). Briefly, yarn bundles (17 multi-filament yarns per yarn bundle) were produced from multi-filament yarns comprising of 30 filaments/yarn of silk. The resulting structure was made such that yarns were oriented at 32° angle to the long axis of the braid using a production rate of 1 meter/min to produce braided structures. The 3D braids were manually cut into smaller structures approximately $4 \times 2 \times 1 \text{ mm}^3$ dimensions.

2.3 SBF immersion

Post fabrication, silk fibroin 3D matrices and films were immersed in $1.5\times$ SBF solution for 7 days. SBF ($1.5\times$) solution was prepared as described elsewhere under constant stirring at 37 °C and buffered at pH 7.4 using 75 mM Tris buffer [25]. Alternatively, an equal number of matrices (films, lyophilised and braids) were immersed in 2 kmol/m³ of CaCl₂ and incubated for 24 h at 37 °C [26]. Then the matrices were very gently washed with deionized water and air dried prior to immersion in $1.5\times$ SBF. The temperature of the solution was maintained at 37 °C until the matrices were immersed. The samples were harvested after 7 days for analytical purposes.

2.4 Analytical Techniques

2.4.1 Micro-CT

To quantify 3D morphology, silk fibroin matrices were characterized using X-ray micro-CT (Nano-focus, Phoenix X-ray GE, Measurement & Control, Wunstorf, Germany). The conditions used were an accelerating voltage of 55 kV, 120 μ A current and 1000 projections over 360°. Three 2000 ms projections were averaged per angle to reduce noise. All materials were scanned at low (20 μ m voxels) and high (3.5 μ m) resolutions. The resulting 3D volume images were then processed using an edge-preserving filter to remove noise and artefacts, followed by segmentation to allow 3D quantification. Three quantitative assessments were performed, as described below.

The specific surface area (**SSA**) was calculated by dividing the surface area of matrix (SA_{matrix}) by its volume (V_{matrix}) [27]:

Tortuosity was calculated by dividing the line length between two points and the distance between the loading platens. [28]

Porosity was calculated by the volume of non-matrix materials by the total volume in the field of view [29]:

where VB is the volume of binarized object (matrix material phase) in volume of interest (VOI).

2.4.2 Attenuated total reflectance-fourier transform infrared spectroscopy (ATR-FTIR)

ATR-FTIR spectra of silk fibroin matrices including films, lyophilised and braids ($n = 3$ per group) before and after treatment were obtained using an Alpha-P spectroscope (Bruker, USA).

A total of 72 scans were taken in absorbance mode in the spectral range of 4000 to 500 cm^{-1} for each measurement at data acquisition rate of 4 cm^{-1} per point. Spectral analysis was performed for relative comparison. Deconvolution was done on the spectra using Fourier self-deconvolution (FSD).

2.4.3 Atomic Force Microscope (AFM)

Surface roughness of silk fibroin matrices (films, lyophilised and braids) treated with SBF with or without CaCl_2 pre-treatment as well as untreated controls ($n = 3$ per group) were imaged using Digital Instruments Nanoscope in contact mode. Three randomly chosen areas of 10 $\mu\text{m} \times 10 \mu\text{m}$ dimensions were imaged and the mean of their respective surface roughness (Rq) values was calculated. In the case of braids, roughness of a single fibre was measured as the presence of grooves in braided structures does not permit probe detection of the surface.

2.4.4 X-Ray Diffraction (XRD)

X-ray diffraction was performed in a Siemens type F X-ray diffractometer using Ni-filtered Cu KR radiation (30 kV, 20 mA, $\lambda = 0.154$ nm) as the source. For scanning, the materials were loaded onto the aluminum frames and scanned from 10 to 50° (2θ) at 2.0°/min.

Particle mean crystallite size (D) was calculated from the XRD data using Scherrer equation [30];

$$= \frac{\lambda}{0.9 \cos \theta}$$

where λ is the wavelength of CuK α i.e. 1.54 nm, β refers to the full width at half-maximum of HA (211,002 planes) and θ is the diffraction angle. The intensity ratio of the preferred crystal-line phase of HA was also calculated.

2.4.5 Scanning Electron Microscope (SEM)

Ultrastructural analysis of the matrices (films, lyophilised and braids; n = 3 per group) either treated or untreated controls, were imaged for identification of apatite deposition. For SEM analysis, fixed samples were thoroughly rinsed in DI water followed by dehydration through graded alcohol series. Air dried samples were then sputter coated with gold (upto 15-20 nm thickness) using an EMITECH K550X (UK) sputter coater set at 25mA for 240 seconds. The coated samples were imaged at varied magnifications using a JEOL 5610LV (JEOL; Japan) SEM at an accelerating voltage of 5 kV.

2.4.6 Energy dispersive X-ray emission (EDX)

To confirm the elemental composition of surface deposition on the matrices (n = 3 per group), EDX analysis was performed on carbon coated samples. Imaging was performed using Zeiss

EVO 50 high definition SEM and the respective Ca/P ratios were computed from the EDX spectrum.

2.4.7 Transmission electron microscopy

For ultrastructural analysis, silk matrices ($n = 3$ per group) were processed as described elsewhere [31]. Briefly, the matrices were ultrasonically dispersed in ethanol followed by deposition onto carbon-coated grids in dilute suspensions and scanned at 200 kV (JEOL 2000 FX-II) with images captured on Kodak DEF-5 film. For characterization of the crystalline deposition, high resolution phase contrast imaging of the samples was performed. From the captured images, interplanar distance and aspect ratio of the deposited HA was determined using ImageJ software.

2.5 Statistical analysis

Statistical analysis was performed using Student's t test and results with $p \leq 0.05$ were considered to be statistically significant. The data obtained from measurements of surface roughness, α -sheet content and aspect ratio were expressed as mean value \pm standard error mean.

3. Results

3.1 Physical Characterisation

The matrices were characterized by different techniques to gain insight into their morphology, surface chemistry, specific surface area, porosity, topography and secondary conformation with potential relevance in the extent of mineralisation induced. SEM micrographs from a single representative image of film, lyophilised and braid (insets displaying digital camera images) is shown in **Figure 1A**. 2D planar films demonstrated a smooth surface morphology with no pores on the surface, whereas the lyophilised and braided structures appeared relatively rougher due to the presence of pores, random porosity and interconnectivity.

By applying micro-CT imaging algorithms, 3D reconstructions of the structures (lyophilised and braids) were obtained (**Figure 1B**). Qualitatively these images highlight the criss-cross architecture of the braided structures, including (**inset; Figure 1B**) a high resolution of the open porosity in the internal structure, conducive to nutrient perfusion. For the lyophilised materials, the pore walls can be seen to form parallel lamella rather than sphere shapes, with the lamella aligned in several directions within a complex 3D structure. The specific surface area was highest for braids (0.72), decreasing slightly for lyophilised (0.66), whilst both were significantly greater than the films (0.04) (**Figure 1C**). The tortuosity of each material was also calculated from the 3D images using the algorithm [28], a measure which is directly proportional to porosity and inversely proportional to the diffusion coefficient of the samples (**Figure 1C**). The results display a trend similar to specific surface area, with maximal diffusion coefficient for braids and nominal for films.

AFM was used to evaluate the surface roughness of the three surfaces. Results were in accordance with SEM micrographs and depicted a substantial increase (**Figure 2, p<0.05**) in the surface roughness (Rq value) of samples from 2D planar films to 3D porous structures (lyophilised and braids). Braided structures, with 77 ± 5.93 nm Rq value, possessed highest surface roughness amongst all the samples (**Figure 2B**).

To characterize the macromolecular conformation of silk fibroin matrices, ATR-FTIR was performed (**Figure 3**). The infrared spectral absorption for amide I ($1700\text{-}1600\text{ cm}^{-1}$), amide II ($1600\text{-}1500\text{ cm}^{-1}$) and amide III ($1300\text{-}1200\text{ cm}^{-1}$) bands were assigned to C=O stretching, N-H bending and O-C-N bending, respectively [32]. Silk braids, lyophilised and films (**Figure 3A**) showed characteristic peaks for amides I, II and III as shown in **Table 1** below.

Table 1. FTIR analysis of materials

	Amides (cm^{-1})

Matrix Type	I	II	III
Film	1619	1513	1229
Lyophilised	1621	1513	1230
Braid	1621	1513	1229

The infrared spectra of the amide I region was deconvoluted (**Figure 3 C-E**) using Fourier self-deconvolution (FSD) to determine the secondary conformation of each respective material (**Figure 3B**). In braids, the percentage of β -sheet content was 61.5% with 24.6% β -turns (**Figure 3E**). Significantly lower β -sheet content for lyophilised structures was observed which corresponded to 53.4% of β -sheet with about 31% of β -turns (**Figure 3D**), as observed previously [33]. The fraction of β -sheet content within 2D fibroin films was the minimum (p<0.05), comprising of 17.9 % β -sheet (weak) and 58.4% random coils and α -helix (**Figure 3C**). The β -sheets were obtained as a result of ethanol treatment, leading to the formation of water-insoluble structure.

XRD pattern of both lyophilised matrices and braids exhibited characteristic peaks at 20.9° and 24.6° indicating silk II conformation [13]. Broadening of the peaks was observed in all the cases indicating poor crystallinity. In addition, on the basis of selective area diffraction pattern (**Figure 4A**), the polycrystalline nature of the 2D planar films was distinctly evident. However, clear diffractograms of lyophilised and braids could not be obtained due to the bulk nature of the samples.

3.2 Characterization of mineralised matrix

3.2.1 SEM analysis

To determine the morphology of deposited particles on the treated materials post immersion in SBF, SEM was performed (**Figure 5**). The presence of certain low attenuation particles on the surface of all the three samples (braids, lyophilised, films) indicated the presence of surface deposition which spread in a disorderly fashion, but convincingly appeared more aggregated in 3D fibroin materials. An increase in the amount of deposition was noticed when structures were pre-treated with CaCl₂ prior to SBF immersion (**Figure 5 B,E,H**), which was further validated using XRD (**Figure 6**). Overall, more deposition was observed on 3D fibroin matrices compared to 2D planar films, based on visual examination. Three distinctive patterns of HA formation were visible; small nanorods (50-100 nm), oval-shaped spheres (800-1200 nm) and large agglomerates, perhaps formed by the subsequent fusion of nanorods. However, we are not able to reproduce the order in which the sequence of events occurred as only a single time point was considered. Higher magnification images showed that the small nanorods and spheres were mostly limited to the surface of 2D films (with or without pre-treatment with CaCl₂) (**Figure 5 A-C**), whereas 3D fibroin structures depicted large aggregates and agglomerates spread across the material architecture (**Figure 5 D-I**).

3.2.2 XRD

Figure 6 shows the XRD patterns of silk fibroin matrices post-immersion in CaCl₂-SBF for 7 days. No major peak validating HA nucleation on the matrix surface was evident when samples were treated only in SBF solution (**Supplementary Figure S1**). The peaks became more intense upon pre-treatment with CaCl₂, indicating enhanced nucleation and deposition of HA (**Figure 6**) in these groups. The broad halo at $2\backslash$ of 20.2° with a shoulder peak located at 24.6°, attributed to the β -sheet crystalline structure (silk II) of silk fibroin, which was detected in all

the samples [13]. Apart from the peaks corresponding to silk fibroin protein, no other peak was detected in the case of 2D planar silk films in both treatment conditions, suggesting no traces of apatite deposition on films. Hence the XRD data suggests that there is high probability that the deposited low attenuation particles observed on 2D films in SEM (**Figure 5 A-C**) represented amorphous deposition which may have crystallised with time if left in SBF for longer.

In CaCl_2 pre-treated materials, a prominent peak was noticed for braided structures at 31.8° , which corresponded to the characteristic (211) plane of HA according to the standard card of HAP (JCPDS09-0432) (**Figure 6**). Interestingly, an additional peak at 25.8° corresponding to the (002) plane of HA was conspicuous only in braids. The X-ray intensity ratio for (002) to (211) plane of HA on CaCl_2 -SBF treated braids was computed from the XRD diffractograms. The value for intensity ratio ‘I’, where I is $[I(002)/I(211)]$ was greater than 1; significantly higher than the standard intensity ratio [0.4 (JCPDS No. 09-0432)] [34], thus confirming that the HA crystallographic lattice was extended along the c-axis, only in the case of braided structures.

In CaCl_2 pre-treated lyophilised matrices, HA deposition was confirmed displaying the characteristic (211) plane of HA at 31.18° with crystal size of 19.56 nm (**Table 2**), however, the peak exhibited significantly lower intensity compared to braids. Since SBF-treated samples were demonstrating minimal peak intensities (**Supplementary Figure S1**), therefore, only CaCl_2 pre-treated samples were selected for further characterization.

Table 2: Characterization of XRD data

Matrix Type	Pre-Treatment	HA plane	Interplanar distance (d) (Å)	FWHM (deg)	Crystal size (D)
Lyophilised	CaCl_2	211	2.86	4.40	19.56

Braid	CaCl ₂	211	2.80	2.77	31.06
Braid	CaCl ₂	002	3.54	0.60	54.8

3.2.3 AFM analysis

AFM was used to evaluate the surface roughness of the three HA deposited surfaces (**Figure 7**). Results were in accordance with SEM micrographs and depicted an increasing trend in Rq values from 2D films to 3D silk fibroin structures (**Figure 7B**, p<0.05). The surface roughness on braided structures displaying aggregated particles was 162 ± 20.31 nm which significantly decreased to 77.3 ± 10.09 nm in lyophilised structures (p<0.05). Treated films displaying fine, non-aggregated particles on the surface corresponded to a minimum Rq value of 27 ± 5.41 nm.

3.2.4 ATR-FTIR

ATR-FTIR absorbance spectra of treated silk matrices were studied (**Figure 8A**) in order to identify the interaction between silk fibroin and HA. The characteristic peaks for HA observed at 474 cm^{-1} , 562 cm^{-1} and 608 cm^{-1} in both the 3D samples (lyophilised and braids), albeit much sharper in braids, were assigned to the O–P–O bending vibration modes of HA (**Figure 8B**). Positions 1038 and 962 cm^{-1} depicted intense bands in braids due to the P=O stretching of HA, however, absence of this peak at 962 cm^{-1} was noticed in lyophilised matrices. No evident expression was noticed in 2D planar films. In addition, characteristic band at 873 cm^{-1} noticed in 3D silk matrices only confirmed that the phosphate sites were partially replaced by carbonate confirming the nature of the deposition as carbonated HA (**Figure 8B**). Though we used carbonate-free solution in our study [22], the appearance of carbonate peak in apatite is usually an outcome of atmospheric CO₂. However, the presence of this carbonate-specific band could not

be detected in 2D planar films. The band at 632 cm^{-1} indicating the presence of hydroxyl (OH^-) ions in apatitic environment were not conspicuous in both braids and lyophilised structures (**Figure 8B**). Nevertheless, no concrete conclusions can be made based on the absence of OH^- bands as these bands are usually difficult to detect by FTIR spectroscopy in poorly crystallised apatites; reason being that the lower crystallinity of apatite leads to enlarged vibration signals, subsequently masking the weak OH^- bands [4]. Moreover, the apatites formed are nonstoichiometric in nature comprising of calcium and hydroxide vacancies, and therefore whatever little amount of OH^- ions are present are often difficult to detect [4].

Further to this, slight shift in the positioning of amide peaks, commonly known as the ‘blue shift’ [2], was evident in the CaCl_2 pre-treated lyophilised matrices (**Figure 8 a-c**) and braids (**Figure 8 d-f**) validating the strong chemical interaction between silk fibroin and HA. The amide III peak shifted from 1229 cm^{-1} to 1259 cm^{-1} in the case of braids (**Figure 8d**) whereas for lyophilised, the peaks now corresponded to 1236 cm^{-1} from 1230 cm^{-1} (**Figure 8a**); with braids showing a more drastic shift. Moreover, in the amide II region, a shift for 6 cm^{-1} (from 1513 to 1519 cm^{-1}) was observed for lyophilised and 11 cm^{-1} for braids (**Figure 8 b&e respectively**). An interesting observation was the presence of the ‘red shift’ noticed in the braids (**Figure 8f**) which may be ascribed to the interaction between the C=O group of silk fibroin with the Ca^{2+} ions [17]. Overall, the discrete shift in the respective amide peaks was indicative of the formation of new bonds established between Ca^{2+} , C-O and N-H groups and indicated strong chemical interaction between silk fibroin and HA.

3.2.5 EDX

Figure 9 shows the EDX pattern of pre-treated silk fibroin matrices post immersion in SBF. The Ca/P atomic ratio for lyophilised matrix was significantly lesser than 1.67 (**Table 3**); standard atomic ratio of pure HA [35]. This indicates that the deposition observed on the surface of

lyophilised structures was Ca-deficit. On the other hand, the calculated atomic ratio for braids was similar to commercial HA (Sigma, Cat no. 677418) (**Table 3**) suggesting that the calcium phosphate deposition on their surface was mostly crystalline HA. 2D planar films did not exhibit any traces of Ca or P within the detected range.

Table 3: Summary of constitutional Ca and P in treated materials

Matrix type	Ca (weight %)	P (weight %)	Ca/P Ratio
Lyophilised	0.446	0.571	0.78
Braid	27.458	15.686	1.75
HA Commercial	25.338	15.430	1.64

3.2.6 TEM

The (nano)structured crystals formed after 7 days of SBF immersion were further characterized using TEM (**Figure 10**). No obvious HA deposition was visible on films, however, the presence of some spherical-like structures was seen which may be due to the amorphous nature of depositions (**Figure 10A**), as also confirmed by XRD (**Figure 6**). Braided structures demonstrated the presence of aggregated particles deposited along the entire length of the fibres (**Figure 10C**). However, the width of the fibre noticed in **Figure 10C** is very small compared to the typical fibre diameter of *B.mori* (20-30 μm in native form and 7-8 μm post-degumming). Reason may be attributed to the extensive mechanical stress and friction caused by the braiding process which can cause fibrillation in addition to the ultrasonication-induced fragmentation

during sample processing. This might justify the smaller width of the braided fibre observed in **Figure 10C**. Higher magnification of crystals displayed an obvious parallel bundle of structures in both the 3D matrices (lyophilised; **Figure 10B** and braids; **Figure 10 D&E**) which appeared uniform needle-like with approximately 80 nm in length and 20 nm wide. As computed from the captured micrographs of braids, the needle-like structures had an aspect ratio of 8.03 ± 1.01 with predominant lattice spacing of 0.28 nm (**Figure 10E; inset**), corresponding to the (211) plane of HA, also supported by XRD data (**Figure 6**). However, due to the nature of the large aggregates of deposited HA, we were unable to visually identify the (002) plane in braids, which was conspicuous in XRD (**Figure 6**) and selected area electron diffraction SAED (**Figure 10F**). **Figure 10F** shows the SAED image of a treated braid depicting a polycrystalline ring; an outer (211) ring and the inner ring (002) segregated into several small arcs, indicating that the HA formation took place along the crystallographic c-axis (002) longitudinally parallel to fibroin, a mechanism similar to biomineralisation of collagen type I in native bone tissue [2].

4. Discussion

While several studies have reported the role of silk fibroin as an osteogenic template [13,9] and investigated the synthesis and deposition of the HA phase on its surface [2], proper characterization of the deposited HA with respect to the material properties is yet to be explained. Hence lack of sufficient knowledge in this realm poses a significant scientific and technical challenge by impeding the development of biomimetic silk-based matrices for clinical purposes.

Acquiring from the knowledge of recent literature which focuses on the role of intrinsic properties of the underlying matrix, we have fabricated fibroin into different morphologies (film, lyophilised and braid) and subjected them to mineralisation. Textile braids offer dimensional stability (especially torsional) to the structure due to the specific criss-cross network and

preferred orientation of yarns, that may help in modulating the orientation of HA deposition along the fibre, resembling collagen type I matrix of native bone and therefore have potential use as osteogenic constructs. A major finding was that the material properties such as surface roughness, specific surface area, tortuosity and secondary conformation of fibroin changed significantly with respect to the 3D matrix architecture as well as the nature of fibroin (native versus regenerated) and were critical factors in determining selective nucleation and growth of HA on fibroin (**Figure 1**). While the contribution of these intrinsic material properties towards modulating cellular behaviour have been highlighted [3,36], yet their direct implication on the mineralisation potential have not been addressed.

Overall, significantly higher HA deposition in braids and lyophilised matrices suggested that the 3D morphology of the material may be a key factor in deciding the osteogenic potential of fibroin; a phenomenon not observed in 2D planar films (**Figure 1**). This seems obvious, due to the availability of larger hydrating surface area in 3D constructs [3]. However, the availability of surface area may not be the only contributing factor. Another critical factor that may have affected the extent of mineralisation on the fibroin template is the difference in the nature of fibroin template. While the braided structures were prepared from native silk fibres as spun by silkworm, lyophilised matrices and films were prepared by subsequent dissolution of those fibres to develop regenerated structures. The process of regeneration of silk using chaotropic salts drastically disrupts native fibroin macromolecular structure. In a recent study on self-assembly of silk [19], it was observed that under controlled shear rate, native silk solution at 1000 mg/L concentration formed a nanofibrillar structure, bearing structural resemblance to native silk fibres. Regenerated silk solution, on the other hand, produced random aggregates of globular protein under similar shear rate and silk concentration. The primary reason for the differential assembly of the two solutions was attributed to the subsequent fragmentation of the constituted macromolecules or lack of terminal domain dimerisation due to

treatment with chaotropic salts in the case of regenerated silk fibroin [19]. This implies that the intact native structure of the silk fibre in braids offers specific organisation of the amino acid domains for nucleation of HA, which could not be exactly reproduced even in the regenerated matrices due to random aggregated assembly and branching of fibroin network post-dissolution. Hence this may exert influence on the differential mineralisation observed in the 3D matrices (lyophilised vs braids), in spite of having comparable physical characteristics (**Figure 1**).

In vitro nucleation and growth of HA nanocrystals onto organic templates is tightly regulated by the presence of electronegative amino acid groups on the material surface, where the crystal formation originates [37]. Exposure of these different amino acid sites is mainly dependent on the varied surface morphology/architecture of the matrix, which can immensely affect biomineralisation on fibroin. Since the specific surface area (**Figure 1**) as well as →-sheet content (**Figure 3**) was maximal in the case of braided structures in addition to the intact native protein conformation, more Asp groups would be exposed to the surface, hence resulting in distinctive carbonated apatite formation with preferential (002) orientation along the c-axis plane (**Figure 6 & 10**); characteristic of native bone tissue [2]. Moreover, the decreased tortuosity index of the braided structures (**Figure 1**) ensured effective permeability and higher contact with supersaturated solution which would subsequently precipitate Ca and P along the structure. Researchers have also acknowledged the existence of another mineralisation mechanism explicitly established in zebra fish bone [38], as well as in human enamel [39], where the nucleation was initiated not through the ions in solution but *via* an intermediary amorphous calcium precursor. However, lack of sufficient knowledge in this realm makes the generality of this pathway debatable [40,41].

SEM analysis confirmed the presence of certain low attenuation depositions on the material surface with a more aggregated organization on 3D matrices whose Ca/P ratio was close to commercial HA [35] (**Figure 9**), while the films depicted more individually scattered nano-

particles (**Figure 5**). According to FTIR analysis, there was a discrete shift observed in amide peaks when the untreated matrices (braids and lyophilised) were compared to CaCl₂-SBF treated groups confirming strong chemical interactions between HA-silk fibroin (**Figure 8**). This result also highlighted an important aspect of the mechanism underlying mineralisation indicating the involvement of amide groups in the origin of nucleation of HA nanocrystals; as observed previously by others [2]. The presence of impurities such as carbonate have frequently been detected along with HA and is therefore used as a criterion for HA characterisation [42], as detected in braids and lyophilised structures. The TEM images demonstrated that the fibroin could direct the assembly and nucleation of HA nanocrystals along the template (**Figure 10**). The typical needle-like morphology of HA crystals was well represented on 3D morphologies only, with aspect ratio measurements of nanocrystals close to that of synthesized HA [43]. The SAED images indicated a polycrystalline diffractogram for braided structures [34] (**Figure 10**) with preferential orientation extending along the c-axis, as also confirmed from the values of intensity ratio (**Figure 6**). This preferential orientation of the deposited crystals along the c-axis of the template is a typical feature of calcium phosphate noted in human bone and dentin where the c-axes of HA crystals align parallel to longitudinal axis of type I collagen fibrils [44]. This was further confirmed from the Scherrer Equation for XRD suggesting that HA crystal formed on braids was located on the template surface (**Figure 6**) with high probability of (002) crystal face matching well with spatial configuration of the fibroin template. Further, the broadening of the (002) and (211) peaks corresponding to HA suggested poor crystallisation in the case of braids and lyophilised similar to organic-inorganic interactions in bone physiology [2].

In native bone tissue, the structural integrity of bone is a tightly regulated process controlled by coordinated mechanism of collagen synthesis by osteoblasts and their subsequent

mineralisation by poorly crystalline HA [45]. The crystal morphology of needle-like nanocrystals obtained on fibroin in our study was similar to the dimensions found on collagen-HA, as reported by previous studies [46]. Also the immense structural resemblance between the two fibrous proteins; silk fibroin and collagen, raised several questions on their relatable mechanism on regulating the HA crystal growth. In a comparative study conducted to compare the mineralisation potential of single-templates; collagen-HA and fibroin-HA and bi-template; collagen/fibroin-HA, it was revealed that crystallite growth orientation along the preferential c-axis of HA occurred in both the templates, similar to native bone while FTIR confirmed the chemical interaction between HA with fibroin or collagen in single- and bi-templates suggesting their similar osteogenic potential [46]. A cell-independent mechanism described crystal growth of HA on collagen, whereby non-collagenous proteins present within the gap zones of collagen template direct mineral nucleation from ions in physiological solution [45]; a similar mechanism has also been experimentally proven for fibroin by Marelli *et al.* [20] Due to the lack of concrete evidence and sufficient literature, aspects of apatite formation on fibroin are much less understood, however, the assistance of β -sheet secondary conformation in the fibroin mineralisation is relatively well characterized [41]. This phenomenon was also evident in our study whereby the significantly higher β -sheet content found in the case of 3D structures probably played a crucial role in directing the nucleation of HA nanocrystals along the fibres. However, the differential mineralisation amongst the two 3D fibroin constructs (possessing comparable β -sheet content) could only be justified by taking into account the nature of the fibroin template used (native versus regenerated) as explained earlier.

Template-induced nucleation and growth of nanocrystals, similar to the organic template of native bone (collagen type 1), is a vital pathway for determining the structural relevance of fabricated materials. Several nucleation mechanisms to regulate crystal growth on

such organic templates have been proposed [2,36,41]. Nevertheless, the most commonly accepted theory of crystal formation stems from the inorganic ions in supersaturated solutions (such as SBF), which get adsorbed onto the templates in a precisely arranged crystallographic order, under controlled pH microenvironment. The process of matrix-mediated mineralisation in the living systems especially focusing on the role of specific amino acid sequences and secondary conformation of proteins influencing the nucleation aspect of calcium phosphate crystals has been reviewed [42]. In accordance with previous literature, we hypothesize that the nucleation and growth of the HA crystals was assisted by the fibroin template where the extent of mineralisation was dictated by the specific interactions between the crystal plane of HA and the specific 3D arrangement of the fibroin template. In this study, we used SBF solution at pH 7.4 (greater than pI of fibroin; pH 4.5), which facilitated the precipitation of local Ca^{2+} ions from SBF solution into the β -sheet structure of fibroin matrices (containing hydrophilic groups such as $-\text{NH}-$ and $-\text{COO}-$ chains of acidic macromolecules, especially aspartic acid) [37]. Once the Ca^{2+} ions were bound to the fibroin template, the electrostatic interactions attracted $(\text{PO}_4)^{3-}$ and OH^- groups to further assimilate more Ca^{2+} from the solution for promoting nucleation of HA along the β -sheet assembly of fibroin chain; as stated by the double layer theory of calcium phosphate precipitation [47]. Hence the three-dimensionality of the underlying matrix (that aligns and probably distributes the anionic groups in specific 3D arrangement) and tortuosity (that dictates the contact of SBF solution to the organic template; **Figure 1**) are critical factors that may affect the subsequent nucleation process. In addition, the larger the surface area (**Figure 1**), the more probability of ion exchange will occur between the organic template and the ions in solution to facilitate enhanced HA deposition. Another factor that affects HA nucleation on the fibroin surface is the interfacial structure. HA will be extended along a particular direction only when the interplanar distance of HA fits well with the spacing between

the amino acid (which is Asp in the case of fibroin) [2], considering that the formation of fibroin–Ca²⁺ was facilitated by anionic functional groups. Since the distance between Asp molecule i.e. 0.15 nm is close to the distance between Ca²⁺–Ca²⁺ in (002) phase (0.13–0.165 nm), HA extended along the c-axis plane, only in the case of braided structures.

Once the nucleation process is initiated, the growth of HA with time on fibroin chains may well be justified by nucleation–aggregation–agglomeration theory [48,49]. Briefly, the deposited nanocrystals are aggregated by molecular attractions [50] which cause subsequent decrease in the surface free energy. Meanwhile, further crystal growth resulted in the formation of agglomerated structures which further led to increased particle sizes by promoting further aggregation of the agglomerated particles (**Figure 5**). Although, the concentration of fibroin is sufficient to further increase the crystal size, simultaneous depletion in the Ca²⁺ ionic concentration limits the resultant crystal size. From the apparent broadening of (002) and (211) peaks and the calculation of Scherrer Equation we can infer a smaller crystal size for 3D fibroin structures (**Table 2**). The biological relevance of this small particle size is that it may aids in solubility of bone by resorbing osteoclasts, as well as maintains the mechanical properties, likely preventing the propagation of cracks [3]. Hence, we can conclude that the HA-fibroin cross-linked together to form the inorganic-organic interactions resembling natural bone, though only when the fibroin template was natively spun in braided morphology.

However, one limitation of our study is that for a more direct comparison between native versus regenerated silk fibroin, it would have been ideal to compare identical morphologies. But it is not possible to fabricate braided structures post-dissolution of cocoons. Taken together, braided structures prepared from native *B.mori* silk demonstrated improved HA deposition. The specific orientation of the yarns and structural stability of the network will play a critical role in determining the mineralisation potential. Lyophilised matrices, prepared by subsequent dissolution of fibres, though possessing comparable β -sheet content, demonstrated

relatively lesser mineralisation. Changes in the extent of mineralisation with the method of processing implied that the growth and nucleation of nanocrystals is template-induced guided by the intact protein conformation of native fibroin. Hence these findings suggest that the 3D textile technology based structures, such as braids, made up of native silk fibres may provide a suitable template matrix, compared to regenerated silk, for producing hydroxyapatite-based mineralised materials for bone repair.

5. Conclusions

To gain an understanding of the mechanism of template-induced nucleation and growth of HA nanocrystals on silk fibroin, we have studied the molecular interactions of HA with silk fibroin (native versus regenerated) fabricated in different morphologies. Ca^{2+} ions bound to the natively spun braids trigger mineralisation in the presence of supersaturated solution. The deposited nano-particles of HA interact closely with the intact amino acid chains of native polymer and induce the nucleation of HAP nano-needles with their preferential c-axis orientation with Ca/P ratio similar to native bone composition. Apart from the intact polymer conformation, the intrinsic properties of the material play crucial role in modulating the extent of mineral deposition. Hence we conclude that natively spun silk fibroin braids in part mimic the collagen type I matrix of natural bone and thus may serve as potential bone graft substitutes for bone repair and regeneration.

Acknowledgements

This study was funded by Department of Science and Technology, Science and Engineering Board, India (YSS/2014/000472) and Department of Biotechnology, India. A portion of this work was performed at the Research Complex at Harwell, funded in part by the EPSRC (EP/I02249X/1).

References

- [1] M. Iafisco, B. Palazzo, T. Ito, M. Otsuka, M. Senna, J. Delgado-Lopez, et al., Preparation of core-shell poly(L-lactic) acid-nanocrystalline apatite hollow microspheres for bone repairing applications, *Journal of Materials Science: Materials in Medicine*. 23 (2012) 2659–2669.
- [2] J. Wang, F. Yu, L. Qu, X. Meng, G. Wen, Study of synthesis of nano-hydroxyapatite using a silk fibroin template, *Biomedical Materials*. 5 (2010) 041002.
- [3] J. Gomez-Morales, M. Iafisco, J.M. Delgado-Lopez, S. Sarda, C. Drouet, Progress on the preparation of nanocrystalline apatites and surface characterization: Overview of fundamental and applied aspects, *Progress in Crystal Growth and Characterization of Materials*. 59 (2013) 1–46.
- [4] C. Drouet, Apatite formation: Why it may not work as planned, and how to conclusively identify apatite compounds, *BioMed Research International*. 2013 (2013).
- [5] S.H. Park, E.S. Gil, H. Shi, H.J. Kim, K. Lee, D.L. Kaplan, Relationships between degradability of silk scaffolds and osteogenesis, *Biomaterials*. 31 (2010) 6162–6172.
- [6] X. Hu, S.H. Park, E.S. Gil, X.X. Xia, A.S. Weiss, D.L. Kaplan, The influence of elasticity and surface roughness on myogenic and osteogenic-differentiation of cells on silk-elastin biomaterials, *Biomaterials*. 32 (2011) 8979–8989.
- [7] B. Panilaitis, G.H. Altman, J. Chen, H.J. Jin, V. Karageorgiou, D.L. Kaplan, Macrophage responses to silk, *Biomaterials*. 24 (2003) 3079–3085.
- [8] M. Bhattacharjee, E. Schultz-Thater, E. Trella, S. Miot, S. Das, M. Loparic, et al., The role of 3D structure and protein conformation on the innate and adaptive immune responses to silk-based biomaterials, *Biomaterials*. 34 (2013) 8161–8171.
- [9] J. Melke, S. Midha, S. Ghosh, K. Ito, S. Hofmann, Silk fibroin as biomaterial for bone tissue engineering, *Acta Biomaterialia*. 31 (2016) 1–16.
- [10] M. Yang, W. He, Y. Shuai, S. Min, L. Zhu, Nucleation of hydroxyapatite crystals by self-assembled Bombyx mori silk fibroin, *Journal of Polymer Science Part B: Polymer Physics*. 51 (2013) 742–748.
- [11] J.R. Vetsch, S.J. Paulsen, R. Muller, S. Hofmann, Effect of fetal bovine serum on mineralisation in silk fibroin scaffolds, *Acta Biomaterialia*. 13 (2015) 277–285.
- [12] M.J. Lee, J.B. Park, H.H. Kim, C.S. Ki, S.Y. Park, H.J. Kim, et al., Surface coating of hydroxyapatite on silk nanofibre through biomineralisation using ten times concentrated simulated body fluid and the evaluation for bone regeneration, *Macromolecular Research*. 22 (2014) 710–716.
- [13] H.J. Kim, U.J. Kim, H.S. Kim, C. Li, M. Wada, G.G. Leisk, et al., Bone tissue engineering with premineralised silk scaffolds, *Bone*. 42 (2008) 1226–1234.
- [14] G.S. Perrone, G.G. Leisk, T.J. Lo, J.E. Moreau, D.S. Haas, B.J. Papenburg, et al., The use of silk-based devices for fracture fixation, *Nature Communications*. 5 (2014) 3385.
- [15] R. Kino, T. Ikoma, A. Monkawa, S. Yunoki, M. Munekata, J. Tanaka, et al., Deposition of bone-like apatite on modified silk fibroin films from simulated body fluid, *Journal of Applied Polymer Science*. 99 (2006) 2822–2830.
- [16] F. Lin, Y. Li, J. Jin, Y. Cai, K. Wei, J. Yao, Deposition behavior and properties of silk fibroin scaffolds soaked in simulated body fluid, *Materials Chemistry and Physics*. 111 (2008) 92–97.

- [17] L. Radev, T. Gerganov, H. Georgiev, A. Kolev, V. Vassileva, Silk Fibroin / Calcium Phosphate Silicate Composites : In vitro Bioactivity, International Journal of Materials and Chemistry. 3 (2013) 8–15.
- [18] X. He, X. Huang, Q. Lu, S. Bai, H. Zhu, Nanoscale control of silks for regular hydroxyapatite formation, Progress in Natural Science:Materials International. 22 (2012) 115–119.
- [19] S. R. Koebley, D. Thorpe, P. Pang, P. Chrischooides, I. Greving, F. Vollrath, et al., Silk reconstitution disrupts fibroin self-assembly, Biomacromolecules. 16 (2015) 2796–2804.
- [20] B. Marelli, C.E. Ghezzi, A. Alessandrino, J.E. Barralet, G. Freddi, S.N. Nazhat, Silk fibroin derived polypeptide-induced biominerallisation of collagen, Biomaterials. 33 (2012) 102–108.
- [21] P. Dubey, S. Murab, S. Karmakar, P.K. Chowdhury, S. Ghosh, Modulation of Self-Assembly Process of Fibroin: An Insight for Regulating the Conformation of Silk Biomaterials, Biomacromolecules. 16 (2015) 3936–3944.
- [22] X.D. Kong, F.Z. Cui, X.M. Wang, M. Zhang, W. Zhang, Silk fibroin regulated mineralisation of hydroxyapatite nanocrystals, Journal of Crystal Growth. 270 (2004) 197–202.
- [23] S. Ghosh, S.T. Parker, X. Wang, D.L. Kaplan, J.A. Lewis, Direct-write assembly of microperiodic silk fibroin scaffolds for tissue engineering applications, Advanced Functional Materials. 18 (2008) 1883–1889.
- [24] S. Murab, S. Chameettachal, M. Bhattacharjee, S. Das, D.L. Kaplan, S. Ghosh, Matrix-embedded cytokines to simulate osteoarthritis-like cartilage microenvironments, Tissue Engineering. Part A. 19 (2013) 1733–1753.
- [25] T. Kokubo, H. Kushitani, S. Sakka, T. Kitsugi and T. Yamamuro, Solutions able to reproduce in vivo surface-structure changes in bioactive glass-ceramic A-W, Journal of Biomedical Materials Research. 24 (1990) 721-734.
- [26] A. Takeuchi, C. Ohtsuki, T. Miyazaki, H. Tanaka, M. Yamazaki, M. Tanihara, Deposition of bone-like apatite on silk fiber in a solution that mimics extracellular fluid, J Biomed Mater Res A. 65 (2003) 283-289.
- [27] A. M. Parfitt, Bone Histomorphometry: Standardization of Nomenclature, Symbols and Units (Summary of Proposed System), Bone. 9 (1988) 67-69.
- [28] D.P. Fyhrie, R. Zuel, Directional Tortuosity as a Predictor of Modulus Damage for Vertebral Cancellous Bone, Journal of Biomechanical Engineering. 137 (2015) 011007.
- [29] L. De Nardo, S. Bertoldi, M.C. Tanzi, H.J. Haugen, S. Farè, Shape memory polymer cellular solid design for medical applications, Smart Mater Struct. 20 (2011) 035004.
- [30] L.V. Azaroff, Elements of X-Ray Crystallography, McGraw-Hill, New York. 1968.
- [31] Y. Cai, J. Jin, D. Mei, N. Xia, J. Yao, Effect of silk sericin on assembly of hydroxyapatite nanocrystals into enamel prism-like structure, J. Mater. Chem. 19 (2009) 5751–5758.
- [32] M.P. Ferraz, The role of dialysis and freezing on structural conformation, thermal properties and morphology of silk fibroin hydrogels, Biomatter. 4 (2014) e28536.

- [33] J. Rnjak-Kovacina, L. S. Wray, K. A. Burke, T. Torregrosa, J. M. Golinski, W. Huang, D. L. Kaplan, Lyophilized Silk Sponges: A Versatile Biomaterial Platform for Soft Tissue Engineering, *ACS Biomater Sci Eng.* 1 (2015) 260–270.
- [34] W. Zhang, S.S. Liao, F.Z. Cui, Hierarchical self-assembly of nano-fibrils in mineralised collagen, *Chemistry of Materials.* 15 (2003) 3221–3226.
- [35] M.P. Ferraz, F.J. Monteiro, C.M. Manuel, Hydroxyapatite nanoparticles: A review of preparation methodologies, *Journal of Applied Biomaterials & Biomechanics.* 2 (2004) 74–80.
- [36] D. Terada, Y. Yokoyama, S. Hattori, H. Kobayashi, Y. Tamada, The outermost surface properties of silk fibroin films reflect ethanol-treatment conditions used in biomaterial preparation, *Materials Science and Engineering: C.* 58 (2016) 119–126.
- [37] Y. Li, Y. Cai, X. Kong and J. Yao, Anisotropic Growth of Hydroxyapatite on the Silk Fibroin Films, *Applied Surface Science.* 255 (2008) 1681–1685.
- [38] J. Mahamid, B. Aichmayer, E. Shimoni, R. Ziblat, C. Li, S. Siegel, et al., Mapping amorphous calcium phosphate transformation into crystalline mineral from the cell to the bone in zebrafish fin rays, *Proceedings of the National Academy of Sciences of the United States of America.* 107 (2010) 6316–6321.
- [39] E. Beniash, R.A. Metzler, R.S.K. Lam, P.U.P.A. Gilbert, Transient amorphous calcium phosphate in forming enamel, *Journal of Structural Biology.* 166 (2009) 133–143.
- [40] A. Dey, P.H. Bomans, F.A. Muller, J. Will, P.M. Frederik, G. de With, et al., The role of prenucleation clusters in surface-induced calcium phosphate crystallisation, *Nature Materials.* 9 (2010) 1010–1014.
- [41] F.C. Meldrum, H. Colfen, Controlling mineral morphologies and structures in biological and synthetic systems, *Chemical Reviews.* 108 (2008) 4332–4432.
- [42] G.K. Hunter, Interfacial aspects of biomineralisation, *Current Opinion in Solid State and Materials Science.* 1 (1996) 430–435.
- [43] I.A. Figueroa, O. Novelo-Peralta, C. Flores-Morales, R. Gonzalez-Tenorio, M.C. Pina-Barba, Synthesis and characterization of biocompatible-nanohydroxyapatite crystals obtained by a modified sol-gel processing, *Biomatter.* 2 (2012) 71–76.
- [44] Z. Qiu, Y. Cui, C. Tao, Z. Zhang, P. Tang, K. Mao, et al., Mineralised Collagen: Rationale, Current Status, and Clinical Applications, *Materials.* 8 (2015) 4733–4750.
- [45] S. Boonrungsiman, E. Gentleman, R. Carzaniga, N.D. Evans, D.W. McComb, A.E. Porter, et al., The role of intracellular calcium phosphate in osteoblast-mediated bone apatite formation, *PNAS.* 109 (2012) 14170–14175.
- [46] J. Wang, W. Zhou, W. Hu, L. Zhou, S. Wang, S. Zhang, Collagen/silk fibroin bi-template induced biomimetic bone-like substitutes, *Journal of Biomedical Materials Research - Part A.* 99 A (2011) 327–334.
- [47] M.J. Lochhead, S.R. Letellier, V.Vogel, Assessing the role of interfacial electrostatics in oriented mineral nucleation at charged organic monolayers, *J Phys Chem B.* 101 (1997) 10821-10827.
- [48] A.D. Randolph, M.A. Larson, *Theory of Particulate Processes*, Elsevier, 1988.

- [49] R. Rodríguez-Clemente, a. López-Macipe, J. Gómez-Morales, J. Torrent-Burgués and V. M. Castaño, Hydroxyapatite Precipitation: A Case of Nucleation-Aggregation-Agglomeration-Growth Mechanism, *Journal of the European Ceramic Society*. 18 (1998) 1351–1356.
- [50] J. Gomez-Morales, J. Torrent-Burgues, R. Rodriguez-Clemente, Crystal size distribution of hydroxyapatite precipitated in a MSMPR reactor, *Crystal Research and Technology*. 36 (2001) 1065–1074.

Figure Legends

Figure 1. Series of images showing different material morphologies used in the study; films, lyophilised and braids. **(A)** Top panel: SEM images, insets display low magnification digital images of each matrix type; **(B)** Centre: 3D micro-CT images.; **(C)** Graph showing specific surface area, porosity and tortuosity computed from micro-CT data.

Figure 2. **(A)** AFM analysis for roughness value (Rq) of untreated matrices; **(B)** Quantitative analysis of Rq values. (*) indicates significance, p<0.05.

Figure 3. **(A)** ATR-FTIR spectra of untreated matrices; braids, lyophilised and films; **(B)** Comparative analysis of varied β -sheet content; **(C-E)** deconvoluted ATR-FTIR spectra of amide I region ($1600-1700\text{ cm}^{-1}$) of **(C)** films, **(D)** lyophilized and **(E)** braids. (*) indicates significance of data, p<0.05 for significance.

Figure 4. **(A)** SAED of polycrystalline silk film; **(B)** XRD patterns of braids, lyophilised and films depicted with black lines.

Figure 5. Series of SEM images of pre-treated silk matrices examined after 7 days of SBF immersion. Top panel: SBF-treated matrices; Centre: matrices pre-treated with CaCl_2 ; Bottom: higher magnification of mineral-like deposition on matrix surface. From top to bottom; micrographs denote different treatment conditions within the same group. From left to right; comparison of differential HA deposition between the different morphologies. Material is darker shade of grey and deposition is light gray. Note the formation of mineral-like deposition is higher on 3D morphologies compared to 2D films.

Figure 6. XRD patterns of different silk matrices post CaCl_2 -SBF immersion.

Figure 7. **(A)** AFM analysis for roughness value (Rq) of silk matrices post CaCl_2 -SBF immersion; **(B)** Quantitative analysis of Rq values. (*) indicates significance, if p<0.05.

Figure 8. **(A)** ATR-FTIR spectra treated silk matrices post CaCl_2 -SBF immersion; **(B)** Spectra showing characteristic HA peaks in selected region ($400-1100\text{ cm}^{-1}$); **(a-f)** Peak shift in amide groups of lyophilised **(a-c)** and braids **(d-f)**.

Figure 9. EDX micrographs of treated silk matrices post CaCl_2 -SBF immersion; lyophilised, braid and commercial HA.

Figure 10. TEM micrographs of treated silk matrices post CaCl_2 -SBF immersion. **(A)** Ultrasonicated silk fibroin films showing amorphous-like deposition (inset); **(B)** Lyophilised matrix with typical needle-like HA nanocrystals; **(C-E)** Braids showing single fibre (arrow) with characteristic HA deposition along its length; **(D)** Higher magnification of boxed region in **(C)** showing needle-like HA morphology; **(E)** Higher magnification lattice image showing interplanar spacing (inset), **(F)** SAED of treated braid showing polycrystalline HA deposition.

Figure S1. XRD pattern of silk matrices post-SBF immersion.

Figure 1

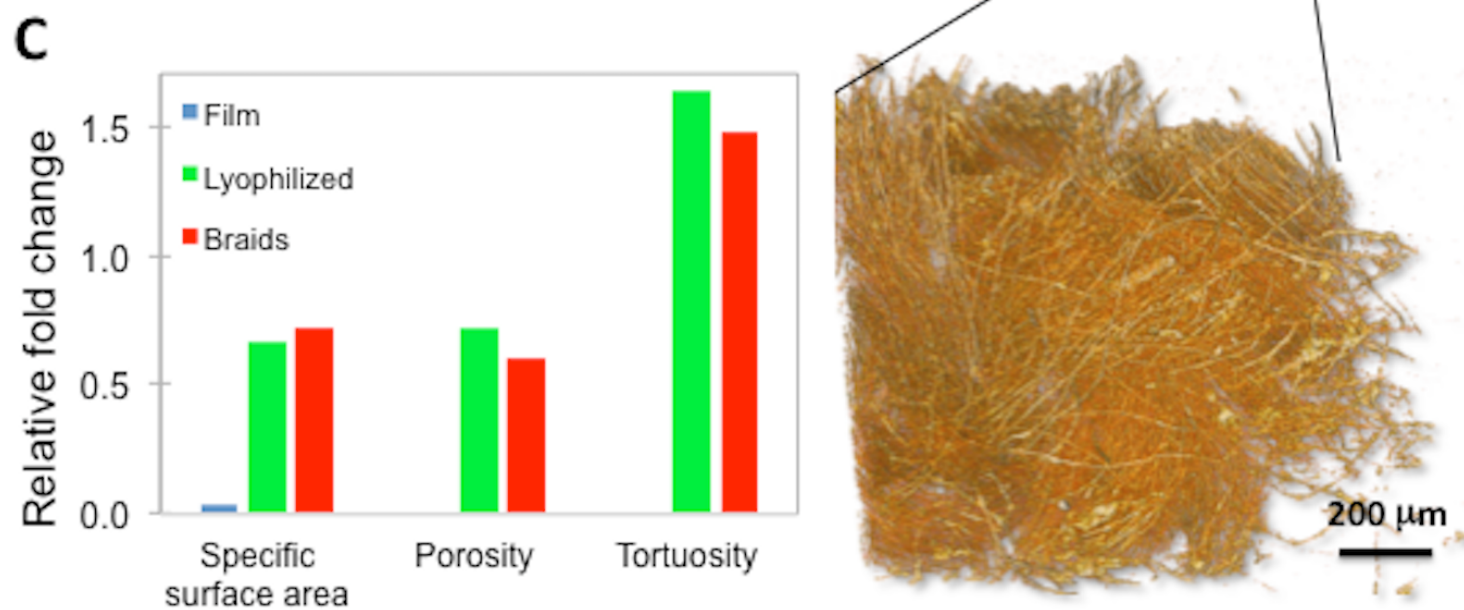
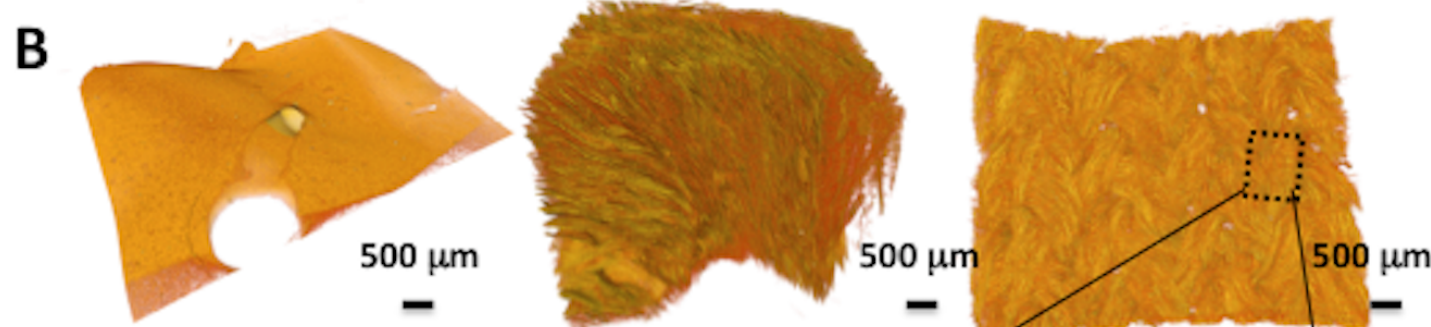
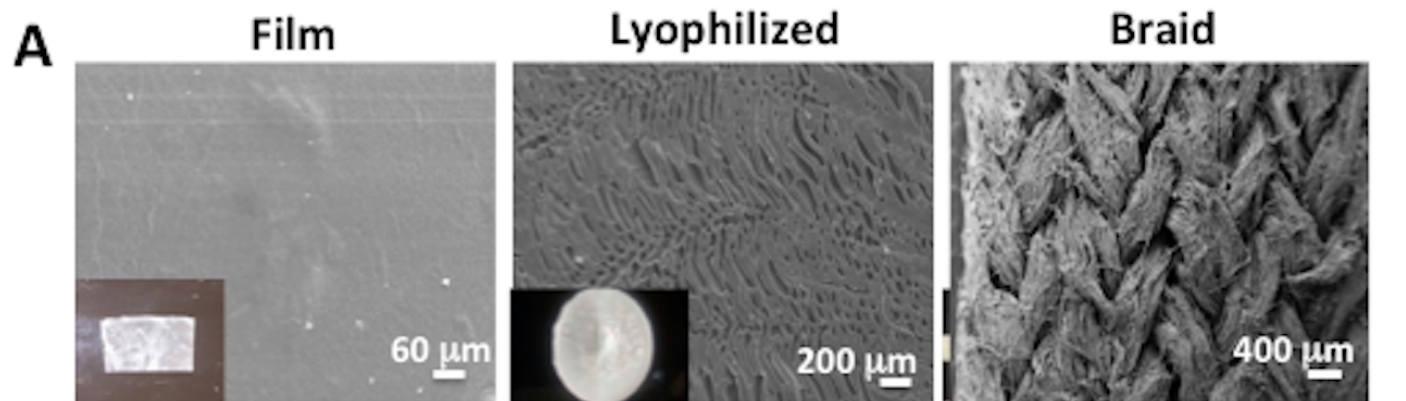
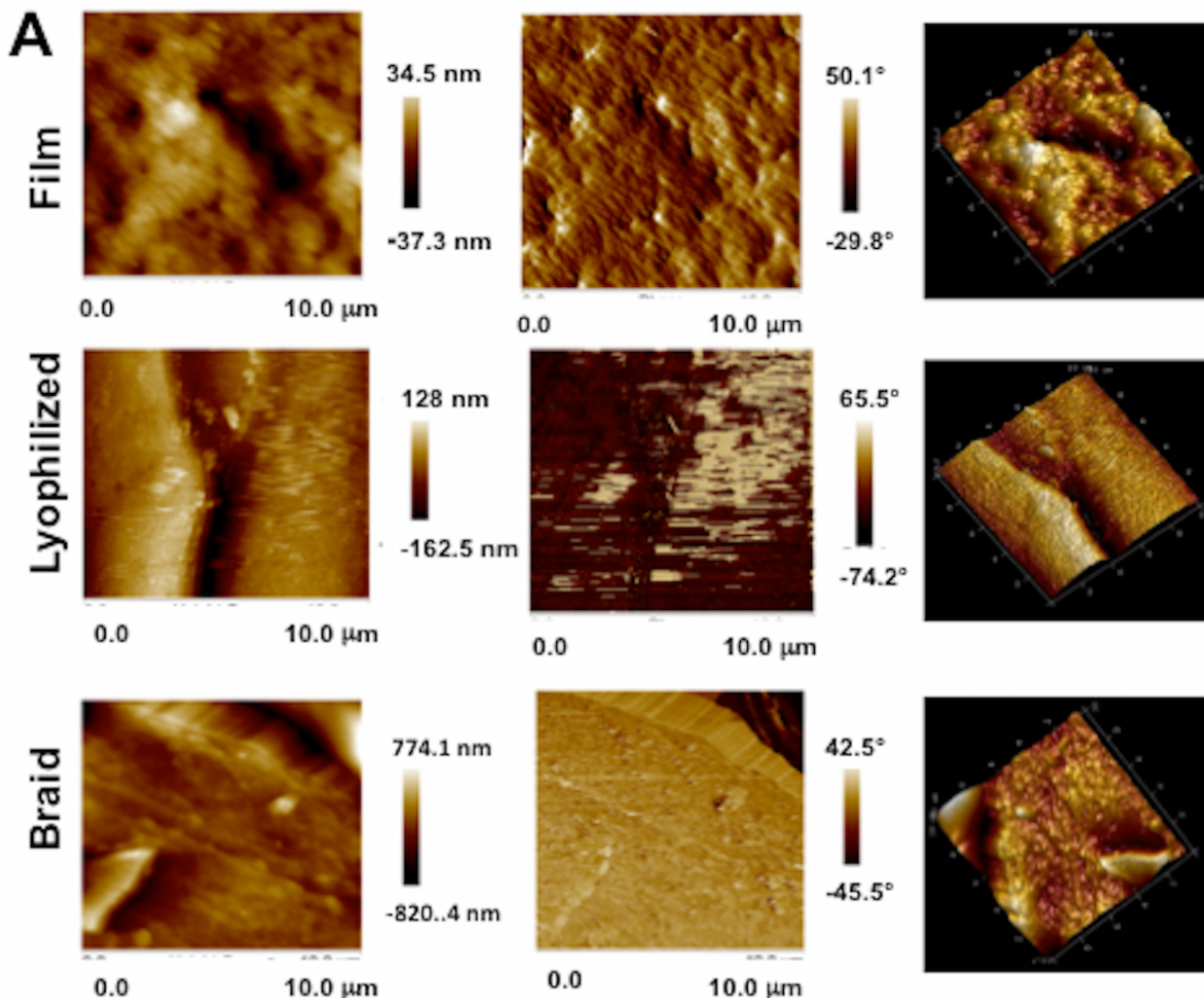


Figure 2



B

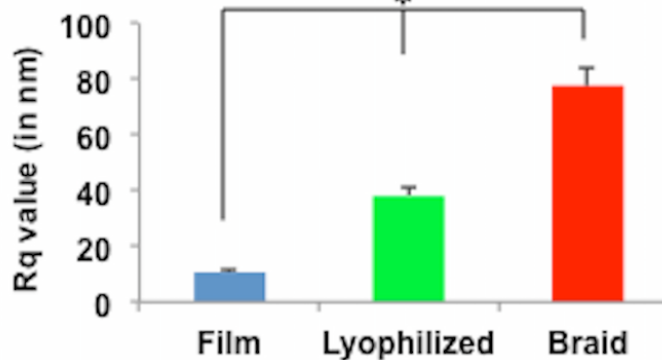


Figure 3

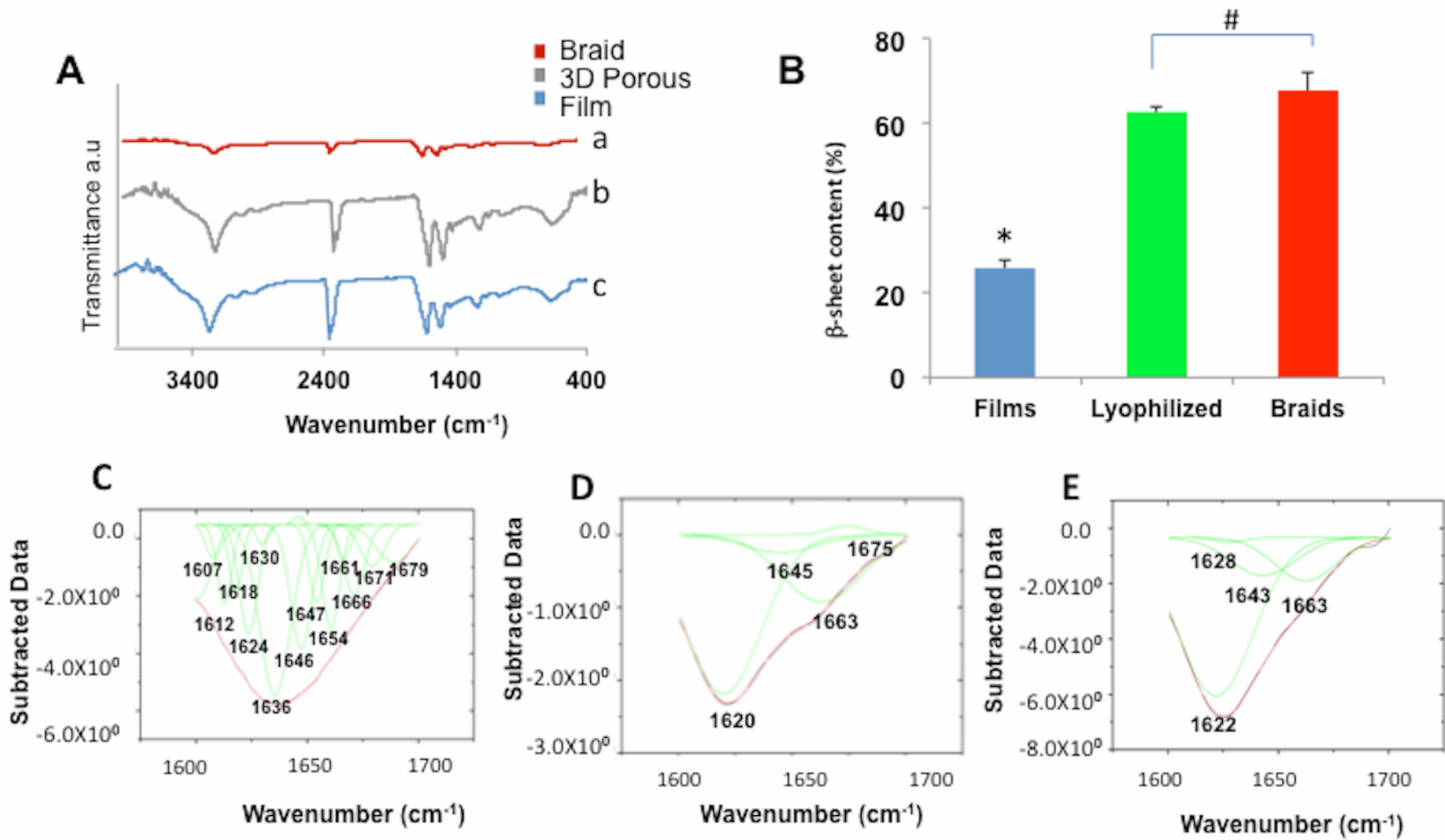


Figure 4

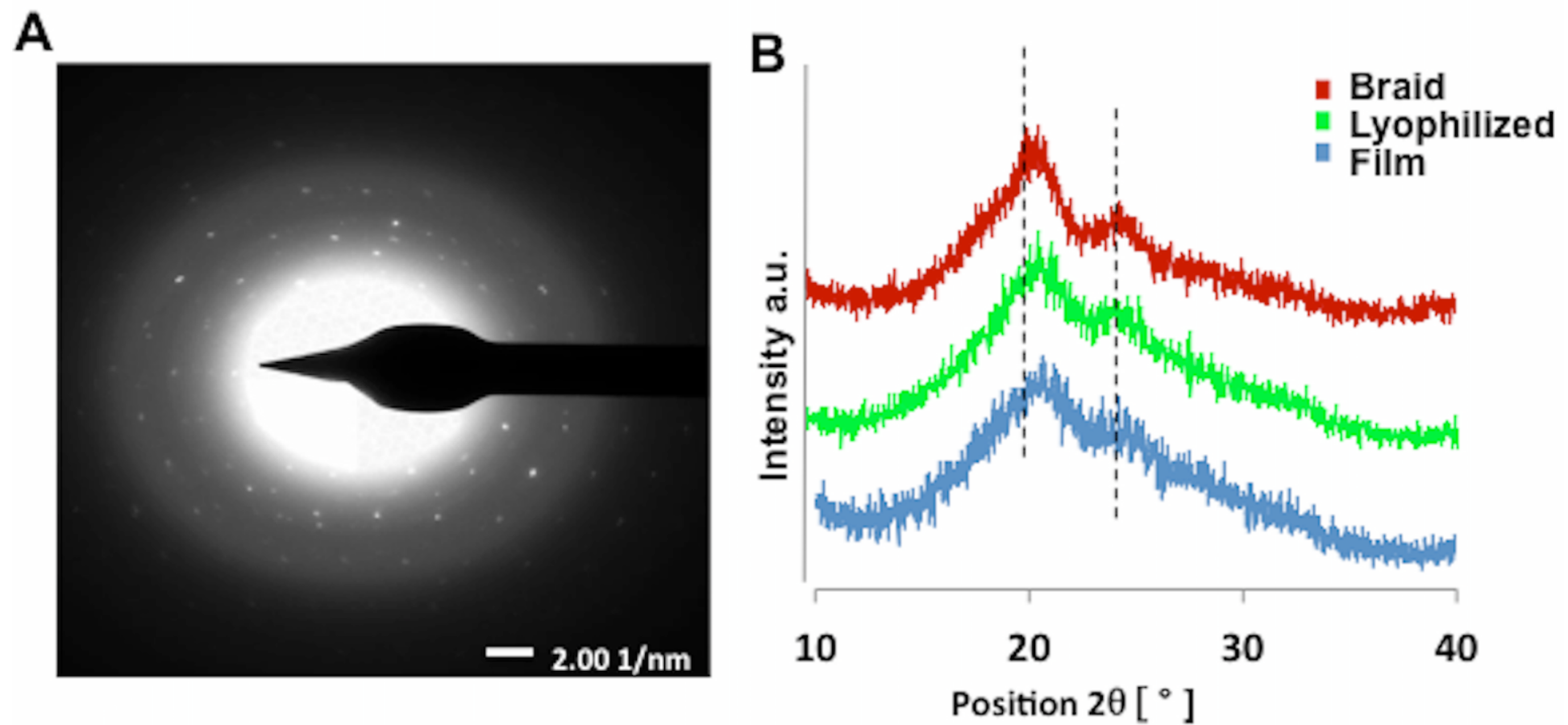


Figure 5

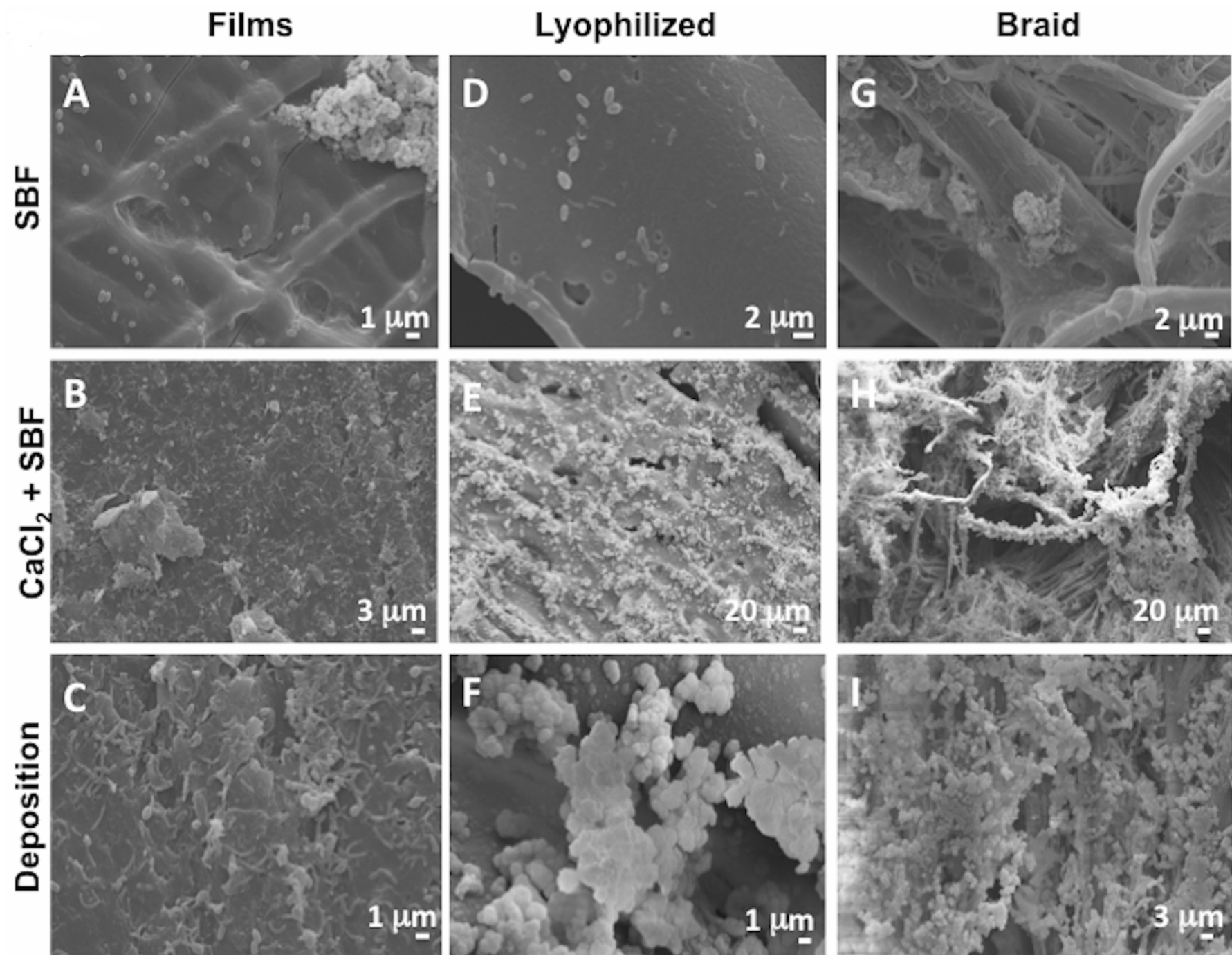


Figure 6

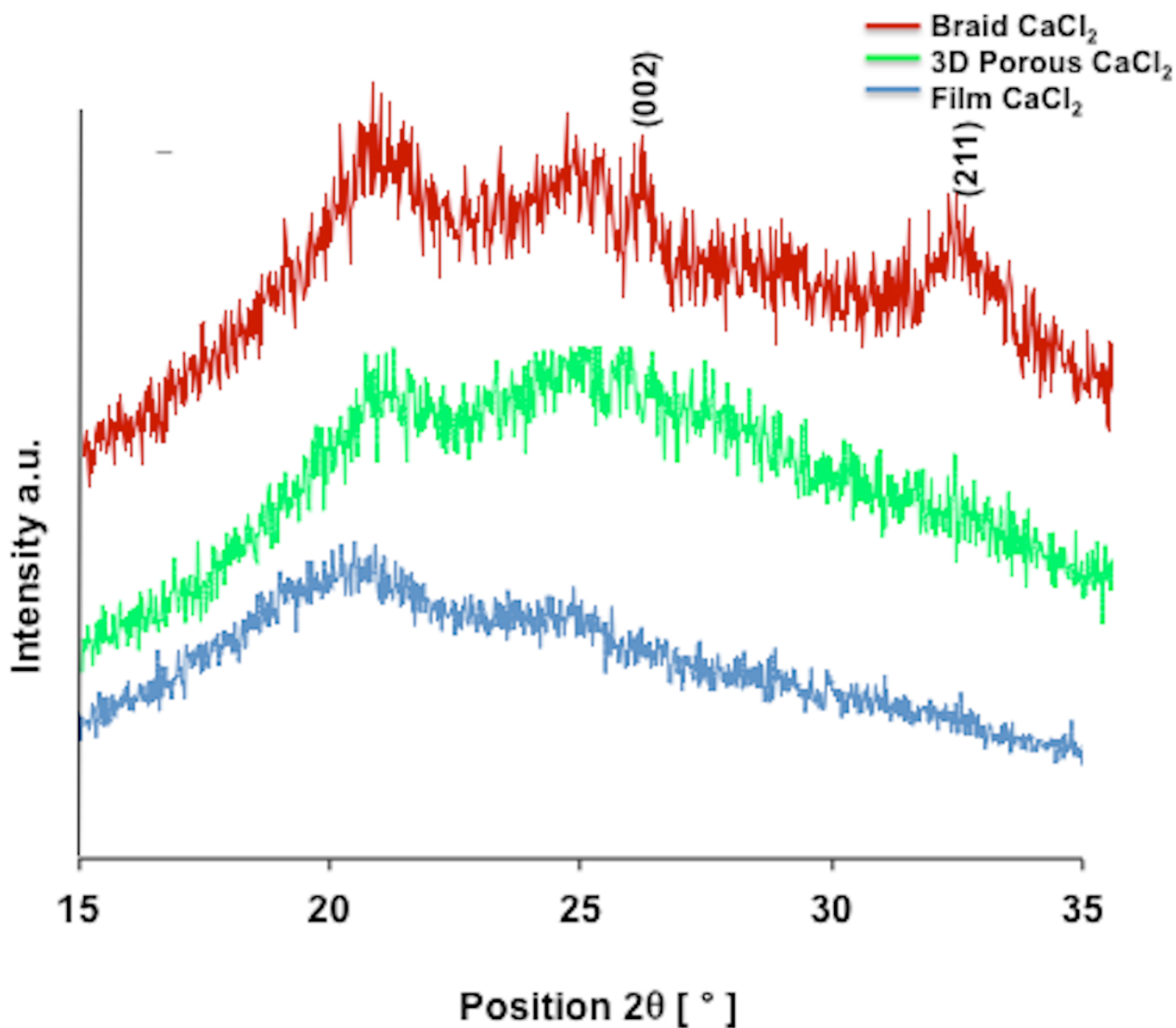


Figure 7

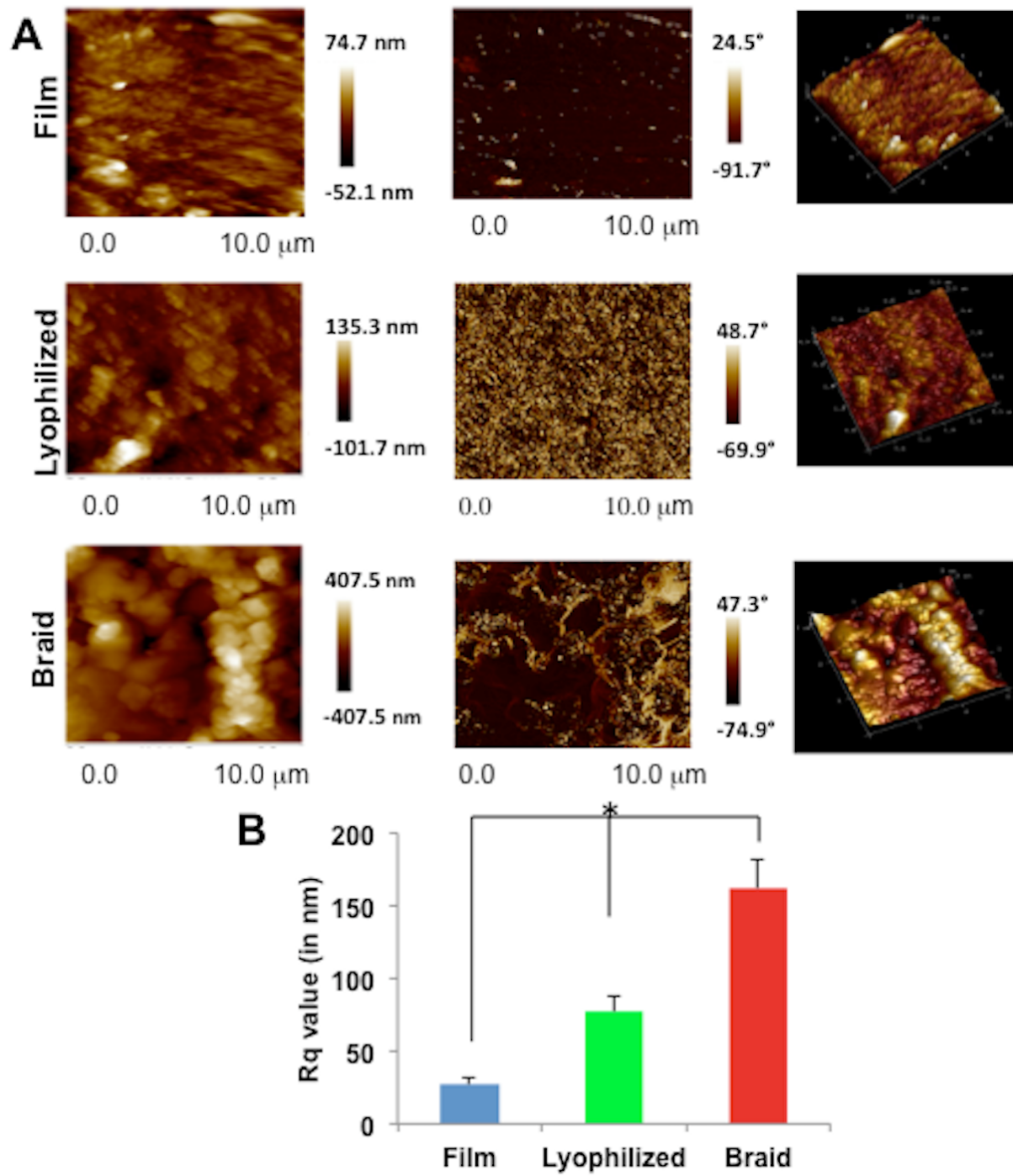


Figure 8

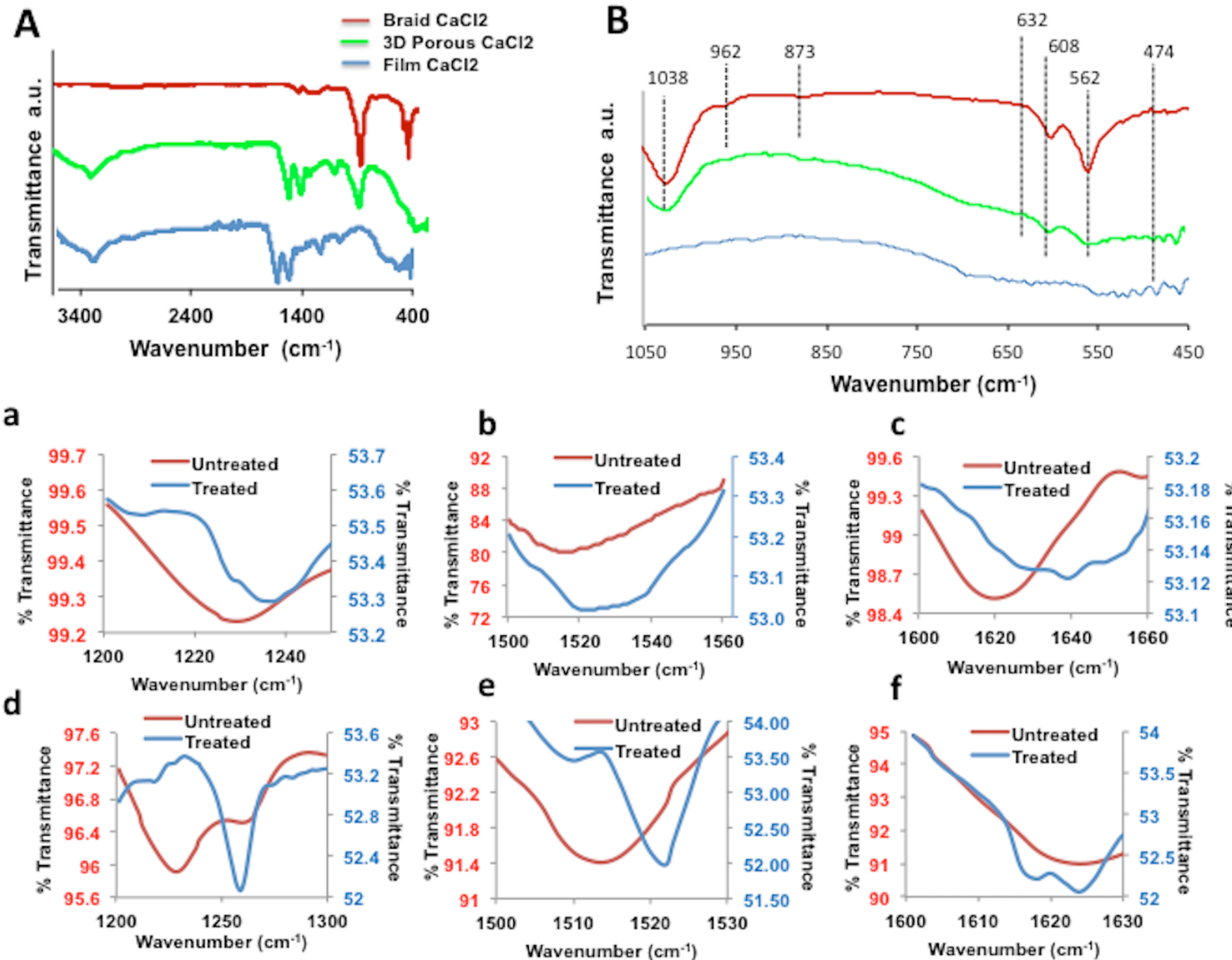


Figure 9

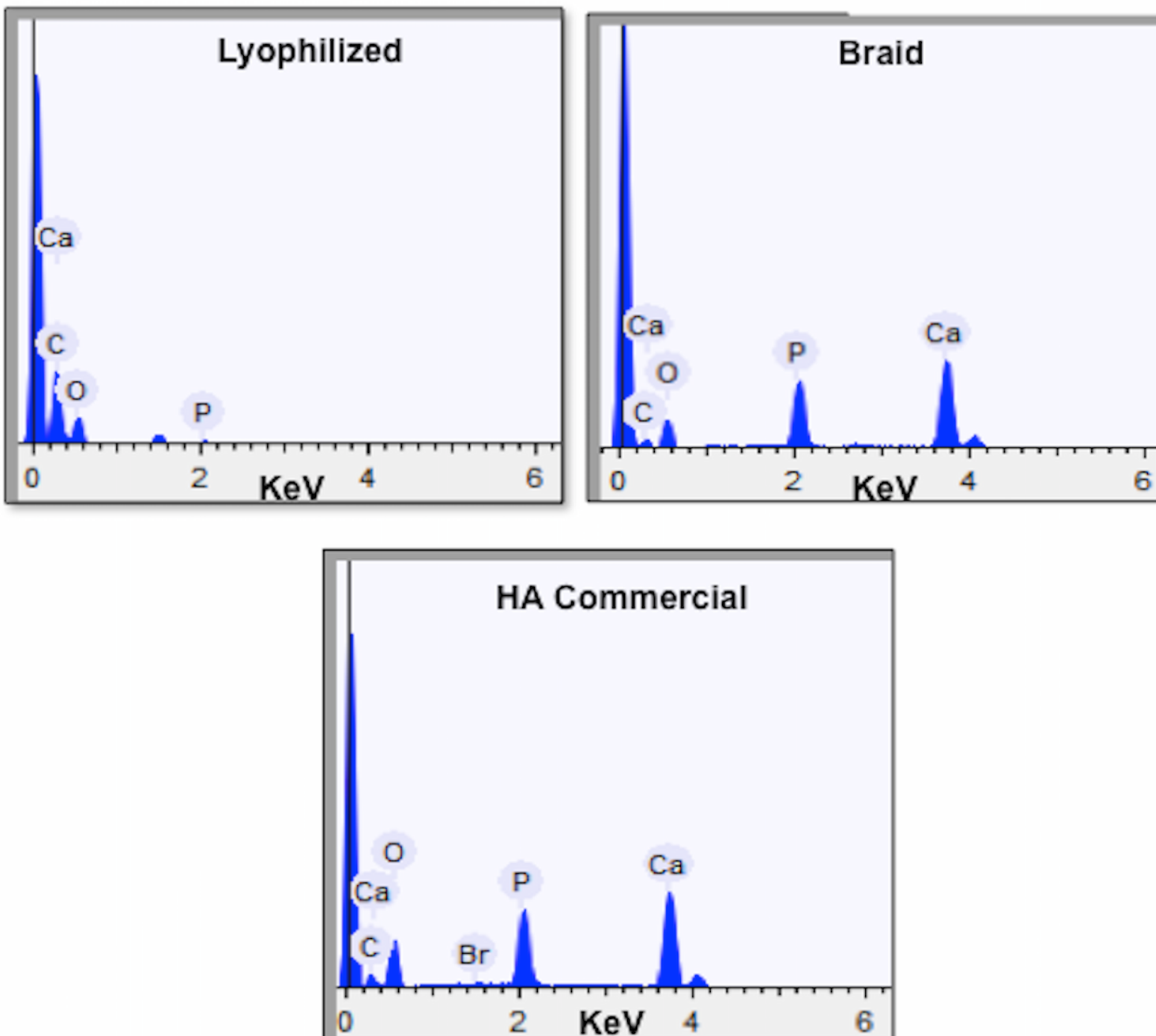
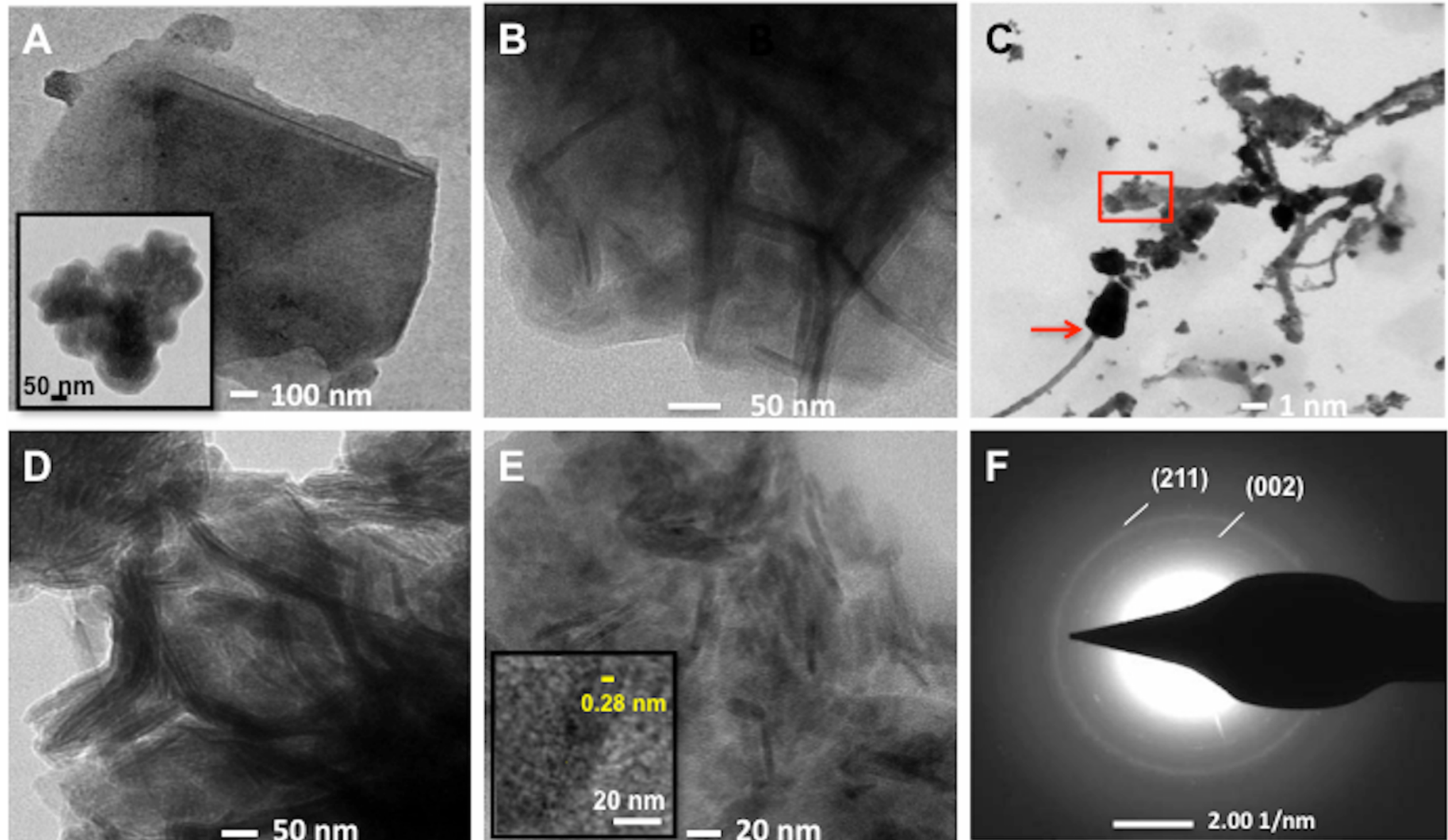
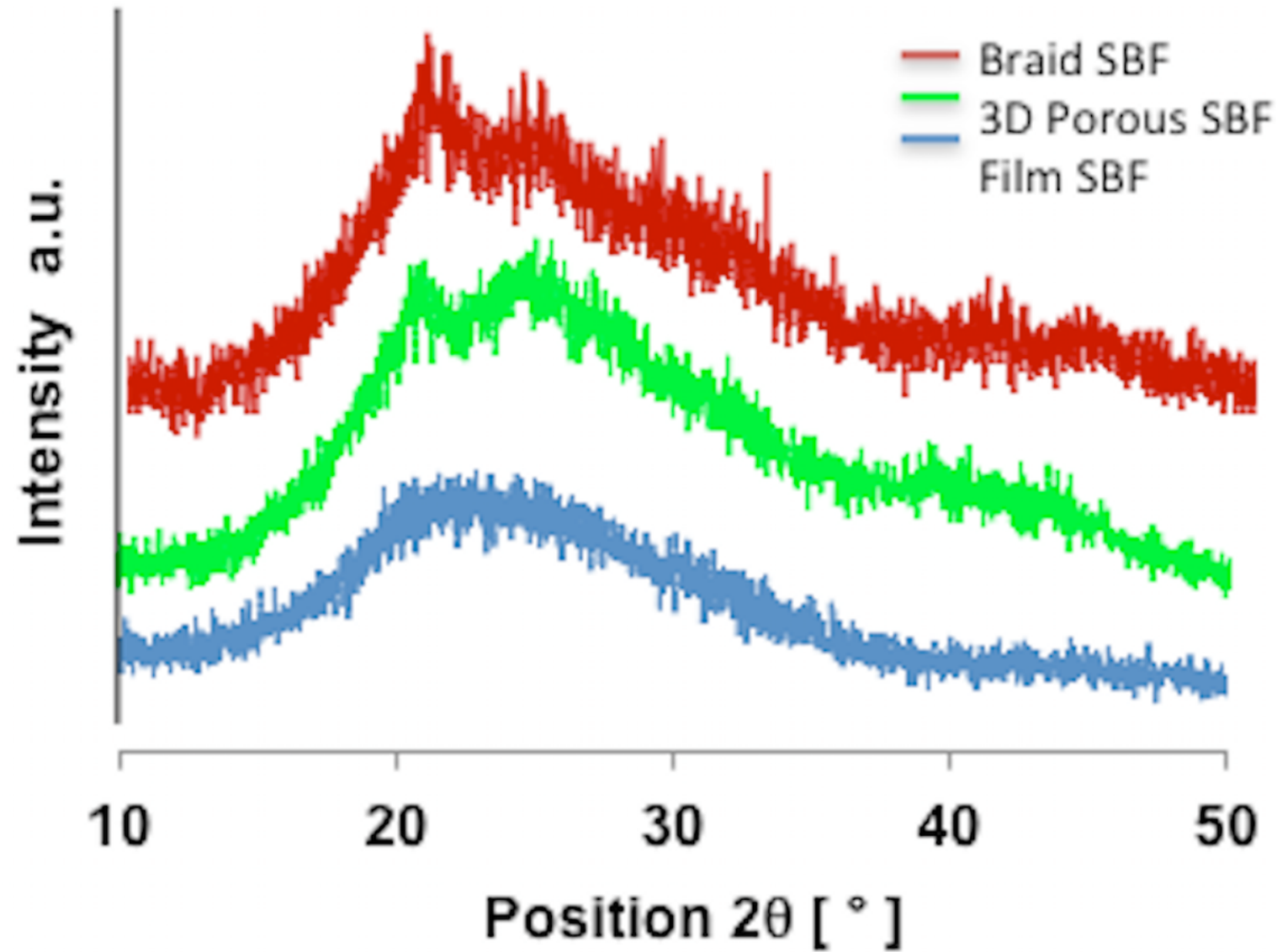


Figure 10



Supplementary Figure 1



Graphical Abstract

